Detection Performance of Upgraded "Polished Panel" Optical Receiver Concept on the Deep-Space Network's 34 meter Research Antenna

V. Vilnrotter[1]

Jet Propulsion Laboratory, California Institute of Technology
4800 Oak Grove Dr.
Pasadena, CA 91109
(818) 354-2745
Victor.A.Vilnrotter@jpl.nasa.gov

Abstract - The development and demonstration of a "polished panel" optical receiver concept on the 34 meter research antenna of the Deep Space Network (DSN) has been the subject of recent papers [1,2]. This concept would enable simultaneous reception of optical and microwave signals by retaining the original shape of the main reflector for microwave reception, but with the aluminum panels polished to high reflectivity to enable focusing of optical signal energy as well. A test setup has been installed on the DSN's 34 meter research antenna at Deep Space Station 13 (DSS-13) of NASA's Goldstone Communications Complex in California, and preliminary experimental results have been obtained. This paper describes the results of our latest efforts to improve the point-spread function (PSF) generated by a custom polished panel, in an attempt to reduce the dimensions of the PSF, thus enabling more precise tracking and improved detection performance. The design of the new mechanical support structure and its operation are described, and the results quantified in terms of improvements in collected signal energy and optical communications performance, based on data obtained while tracking the planet Jupiter with the 34 meter research antenna at DSS-13.

I. Introduction

The option to provide an optical communications capability for the 34-meter microwave antennas of the Deep-Space Network (DSN) is currently under consideration [1,2]. This concept is predicated on the assumption that existing RF capabilities would not be compromised, hence the new optical reception capability should be added without significantly impacting the RF reflecting surfaces, the backup structure, or the pointing requirements on operational DSN antennas. One way to achieve optical communications requirements is to polish the aluminum panels of the antenna's main reflector to optical smoothness, and employ a suitably large detector array to collect the focused light. However, the extent to which thin aluminum panels can be shaped and polished to optical requirements remains to be quantified. This paper documents the results of recent experiments carried out at the Goldstone Communications Complex, designed to evaluate the suitability of polished aluminum panels for optical communications applications.

---

[1] Author is with the Jet Propulsion Laboratory, California Institute of Technology. Copyright 2012 California Institute of Technology. Government sponsorship acknowledged.

As a first step to investigating polished panel performance, two custom aluminum panels with prescribed curvature were procured from Vertex Antennentechnic, GmbH. (Germany), one of which was milled to a mirror-like surface while no attempt was made to polish the other. A custom mounting bracket was constructed, and the polished panel mounted on the main reflector of the 34 meter antenna at DSS-13, as shown in Fig. 1. Note the shallow "grooves" produced by the milling process: these grooves were not removed by re-polishing after the milling operation, and likely impact the ability of this panel to form a small spot at optical frequencies. Plans are to polish the second panel using a different technique to determine if a smoother optical surface can be obtained, and to characterize the potential gain. The location of the polished panel can be seen in Fig. 2a, near the entrance to the RF beam waveguide in the center of the main reflector.

Figure 1. Polished aluminum panel manufactured by Vertex Antennentechnic, Germany, installed on the main reflector of the 34 meter antenna at DSS-13.

In order to evaluate the spot size, or "point spread function" (PSF) generated by the polished panel at its focus, a 10 mega-pixel Finger Lakes Instruments (FLI) digital camera was installed in a weather-proof enclosure equipped with remote-controlled doors at each end for ventilation, mounted next to the subreflector on the movable part of the structure, and controlled from a small room located on the DSS-13 antenna called the "alidade". A picture of the mounted enclosure in the normally closed configuration is shown in Fig. 2b, tilted to point towards the center of the polished Vertex panel. The open configuration, used only during data-gathering, is shown in Fig. 2c where the 2" square narrowband optical filter assembly in front of the FLI camera can be seen.

After installing the camera assembly and routing the control cable to the antenna's alidade, the camera enclosure was activated remotely and nominal operation of the entire system was verified.

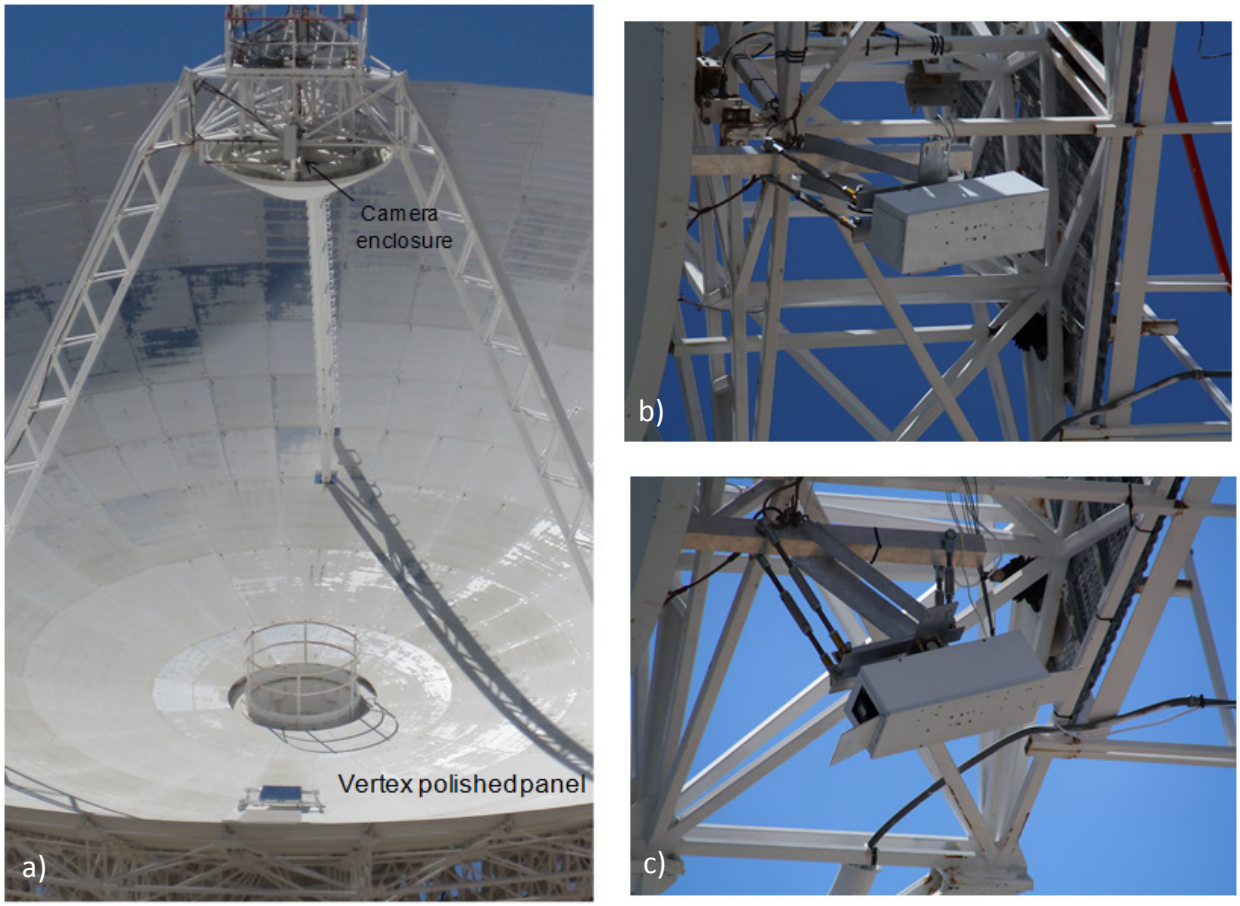

Figure 2. Vertex Polished Panel and FLI camera enclosure mounted on the 34 meter research antenna at DSS-13. a) Vertex polished panel mounted on the main reflector, close to the center; b) FLI camera enclosure mounted on the subreflector backup structure, closed configuration; c) FLI camera enclosure, open configuration.

The enclosure was designed to withstand desert heat, rain and wind with the aluminum doors closed as shown in Fig. 2b, and to quickly cool down during operation with both doors open (Fig. 2c). Although the assembly is always connected to AC power from the subreflector backup structure, the camera and all internal power supplies are activated via relays, which in turn are controlled remotely from the alidade via USB-2 extenders at each end connected via a durable CAT-5 cable running from the alidade through the main reflector and routed through the leftmost tripod in Fig. 2a.

II. Communications Performance Evaluation

In a typical optical communications scenario, the point spread function (PSF) generated by the polished panel would be centered over a photon-counting detector array by applying offsets to the antenna pointing assembly, after which a closed-loop tracking circuit would be activated to remove drifts in the antenna pointing and keep the PSF centered. Temporal acquisition and tracking would then commence to keep the receiver clock synchronized with the symbol-boundaries, as described in [1]. Under these

conditions, detector array processing can be optimized to achieve best performance by sorting the array elements according to energy, and computing the symbol error probability (PSE) for the highest energy detector element, then for the sum of the signal energies in the first two highest energy detectors, and so on, until the minimum PSE is reached. The amount of signal energy collected by the first "m" highest-energy detectors will be denoted by

$$K_s(m) = \sum_{n=1}^{m} \lambda_s(n) \tag{1}$$

where "n" is the order index according to signal energy in descending order. In the following performance calculations the background photon distribution is assumed to be uniformly distributed in the detector-plane, hence the amount of collected background energy increases linearly with m as more detector elements are included. According to this model, the average number of background photons collected by m detector elements is proportional to m, $K_b(m) = m\lambda_b$, where λ_b is the average background photon-count rate per detector element, here assumed to be constant over the array.

Consider the probability of correct symbol detection with pulse-position modulation (PPM) signaling, as described in [1, 2, 3]. For any m, the probability of correct symbol detection is lower bounded by the probability that the photo-count in the correct slot containing the signal-pulse exceeds the count in every other slot within that PPM symbol. For exact results, equalities of maximal counts in any of (r-1) noise-slots ($1 < r < M$) should also be considered, and resolved by tossing a fair r-sided die, but with high average signal and background energies these events are extremely rare and hence can be ignored [3]. The lower bound on the probability of correct detection, $P_M^l(C)$, can be expressed as a function of m :

$$\begin{aligned} P_M^l(C) \geq & \sum_{k=1}^{\infty} \frac{\left(K_s(m) + K_b(m)\right)^k}{k!} \exp\left[-\left(K_s(R) + K_b(R)\right)\right] \times \\ & \left\{ \sum_{j=0}^{k-1} \frac{\left(K_b(R)\right)^j}{k!} \exp\left[-\left(K_b(R)\right)\right] \right\}^{M-1} \\ & P_M^u(E) \equiv 1 - P_M^l(C) \geq P_M(E) \cong P_M(E) \end{aligned} \tag{2}$$

The symbol error probability, $P_M(E)$, is actually somewhat less than predicted by equation (2), but not significantly so. For high background cases the Poisson computations are somewhat time-intensive, hence a much faster Gaussian approximation can often be applied. The Gaussian formula replaces the Poisson probabilities with continuous Gaussian densities whose second-order statistics have been matched to the Poisson distribution, yielding the following equation for the probability of correct detection [3]:

$$P_M(C) \cong \int_{-\infty}^{\infty} dy\, Gsn[K_s(m) + K_b(m), y] \left[\int_{-\infty}^{y} dx\, Gsn[K_b(m), x] \right]^{M-1} \tag{3}$$

Here $GSN(K, x)$ refers to the Gaussian density of the random variable x with mean and variance K. This approximation yields a somewhat pessimistic evaluation of optical receiver performance, but it is nearly exact for the high-signal high-background case we are considering. In the following sections, these

concepts will be applied to determine the minimum probability of symbol error with PPM signaling, using the experimentally determined PSF to generate the signal distribution over a hypothetical photon-counting detector array.

III. Initial Data Acquisition and Signal Processing

Data collected during initial Jupiter observations on September 8th, 2011, consisted of FITS files with 3084X3103 array elements, quantized to 16 bits. The control software of the FLI camera thresholds the pixel values at approximately 2000 out of a total of $2^{16} = 65536$, in order to overcome thermal current and other instrumental effects. Photo-electrons generated by the signal are added directly to this value, generating the "salt-and-pepper" appearance of the original 10 mega-pixel image as can be seen in Fig. 3a, due to the Poisson nature of the photon-counts which are subject to significant fluctuations from one pixel to the next. In order to eliminate the "salt-and-pepper" appearance of the high-resolution image, the pixels were binned into 60X60 pixel subarrays resulting in a 50X50 array where the threshold value was subtracted before binning, hence the binned intensities shown in Fig. 3b now start at zero instead of 2000. No critical information is lost during the binning operation since the extent of the PSF is much greater than the size of the bins, hence the PSF is sampled adequately in both spatial dimensions. Upon closer inspection of the data, it was noted that the first row and first column of the array contained much less signal energy than the rest (likely due to masking of the sensor by the inner edge of the filter assembly), hence the first row and column are deleted in subsequent processing resulting in a 49X49=2401 element array. This smaller array is much easier to process than the original 10 mega-pixel array, while retaining the information needed to characterize the PSF and evaluate the resulting optical communications performance.

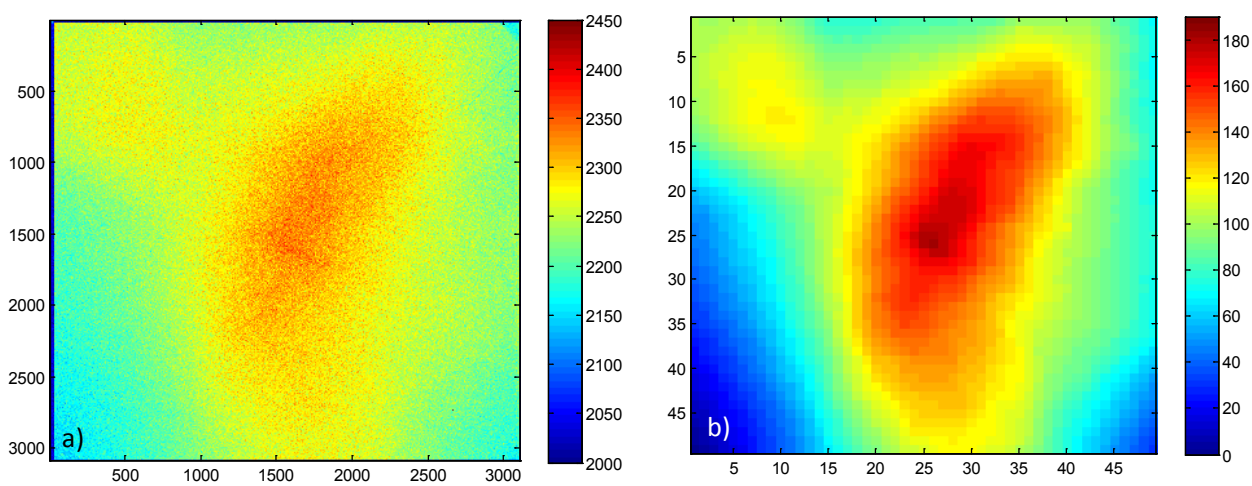

Figure 3. Centered PSF recorded by FLI camera: a) original 10 mega-pixel resolution showing "salt and pepper" pattern; b) smoothed 60X60 binned image showing the spatially averaged structure of the point-spread-function.

When the detector elements are sorted according to signal energy, the distribution of energies shown in Fig. 4a is obtained as a function of the order index "n". Note that all of the 49X49=2401 detector elements contain some signal energy, falling off with increasing order index n due to sorting.

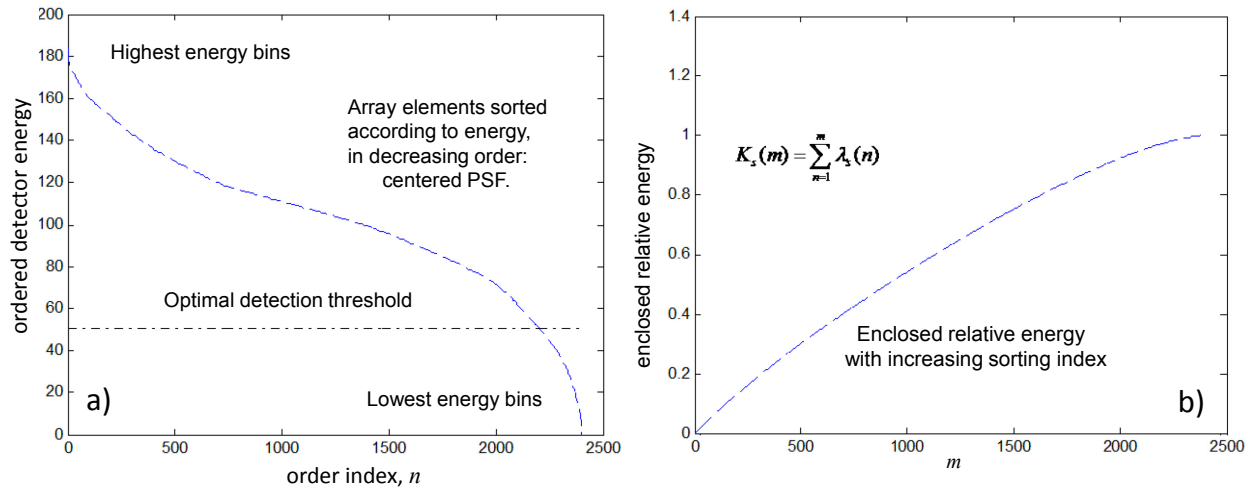

Figure 4. a) Detector elements sorted according to energy, for a centered PSF; b) accumulated relative energy in the first "m" sorted detector elements.

From the viewpoint of optical communications, the most important criterion is detecting and decoding the transmitted data with the highest possible fidelity. This implies the use of advanced detection strategies to achieve the lowest possible symbol-error probabilities consistent with the prevailing operating conditions. As shown in [3], optimal processing of photon-counting detector array data requires optimal weighting of the array elements by a logarithmic factor $w = \ln(1 + \frac{K_s}{K_b})$, which may be difficult to compute and apply in a practical implementation when a large number of detector elements are involved. However, it was also shown in [3] that a simple (1, 0) mask that selects the most favorable detector elements and rejects the rest achieves very nearly the same performance as the more complicated optimal weighting strategy. We shall proceed to analyze the symbol-detection capabilities of a hypothetical optical receiver by applying the optimal (1, 0) mask to a photon-counting array corresponding to the binned subarrays of the large-sensor FLI camera.

Symbol Error Probability Calculations: Assuming that the intensity distribution obtained from the camera is a reasonable representation of the average PSF generated by the Vertex polished panel, we proceed to evaluate communications performance for pulse-position modulation (PPM) with 4 slots per symbol, as described in [1,2].

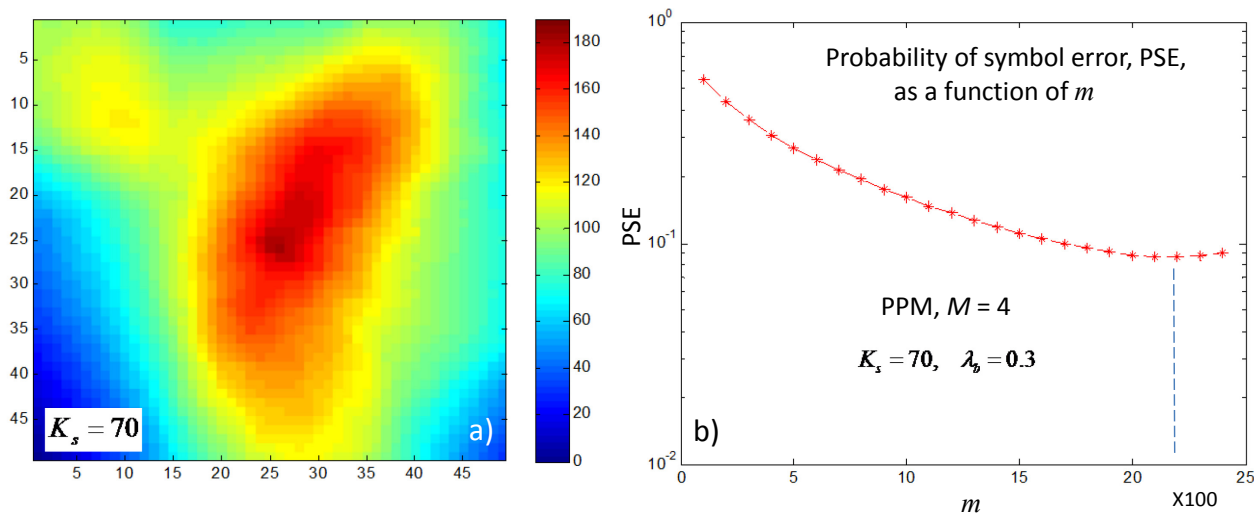

Figure 5. Detection performance of centered PSF: a) binned image representing total average signal count of 70 photons; b) probability of symbol error as a function of *m*, for background counts of 0.3 photons per slot per bin.

The PPM symbol-error probability, PSE, has been computed for the September 8th, 2011 data as a function of m by evaluating equation (3) assuming four slots per PPM symbol so that M=4, assuming total average signal energy of $\Lambda_s = 70$ photons distributed according to the PSF shown in Fig. 5a for illustration purposes, with constant average background count of $K_b = 0.3$ photons per detector element per slot. The computed symbol error probability is shown in Fig. 5b as a function of m, where it can be seen that PSE is minimized by including the 2200 highest-intensity bins: this value defines the optimal detection threshold shown in Fig. 4a, from which the optimal (1, 0) mask can be determined. Note that for this example, nearly all of the signal energy contained within the PSF must be summed in order to minimize symbol-error probability, which only attains a value of $PSE = 9 \times 10^{-2}$ in this relatively high background environment.

The application of the optimal detection threshold shown in Fig. 4a to the array is equivalent to generating a (1, 0) mask that determines which detector elements are to be included in the detection operation. Point-by-point array multiplication excludes the unwanted array elements that contain too little signal energy to help with detection, hence would contribute too much noise and cause the symbol error probability to increasing, as in Fig. 5b for the case m > 2200. Under normal operating conditions, this optimal detection mask must be re-computed and applied in real-time at a rate commensurate with the prevailing atmospheric conditions, to achieve best performance.

IV. Improved PSF via Panel Mounting Upgrades

After the initial data was collected and analyzed, it was determined that significant panel tilt and distortion were present. After this problem was corrected, a dramatic improvement in the shape of the PSF was observed, as can be seen in Fig. 6a (data taken on February 16th, 2012). The signal energy has

now been concentrated into a smaller nearly bell-shaped PSF, as would be expected from a panel with excellent surface figure, but with considerable small-scale surface irregularities which prevented diffraction-limited performance at optical frequencies.

Since the visual magnitude of Jupiter has decreased significantly between September 8th 2011 (when the initial PSF was characterized) and February 16th 2012 when the latest data was collected, it was necessary to correct the measured intensities before quantitative conclusions could be drawn. Each integer increase in visual magnitude decreases the source intensity by a factor of $\sqrt[5]{100} = 2.512$, hence a change of Δm_v in visual magnitude results in a corresponding change of $2.512^{\Delta m_v}$ in observed signal energy. The visual magnitude of Jupiter increased from -2.725 on September 8th 2011, to -2.25 by February 16th 2012, i.e. Jupiter was fading in February relative to September. The change in magnitude between September and February is $\Delta m_v = -2.25 - (-2.725) = 0.475$, which represents a decrease in Jupiter intensity by a factor of $2.512^{\Delta m_v} = 1.55$, which must be taken into account when comparing data taken on these two different dates.

After applying the above correction for the decrease in Jupiter intensity, it can be seen in Fig. 6c that the maximum pixel intensity has more than doubled as a result of the recent panel structure upgrades (from 190 intensity-units to approximately 440), and the total signal energy has increased by a factor of 1.8, from the initial configuration (Fig. 6d).

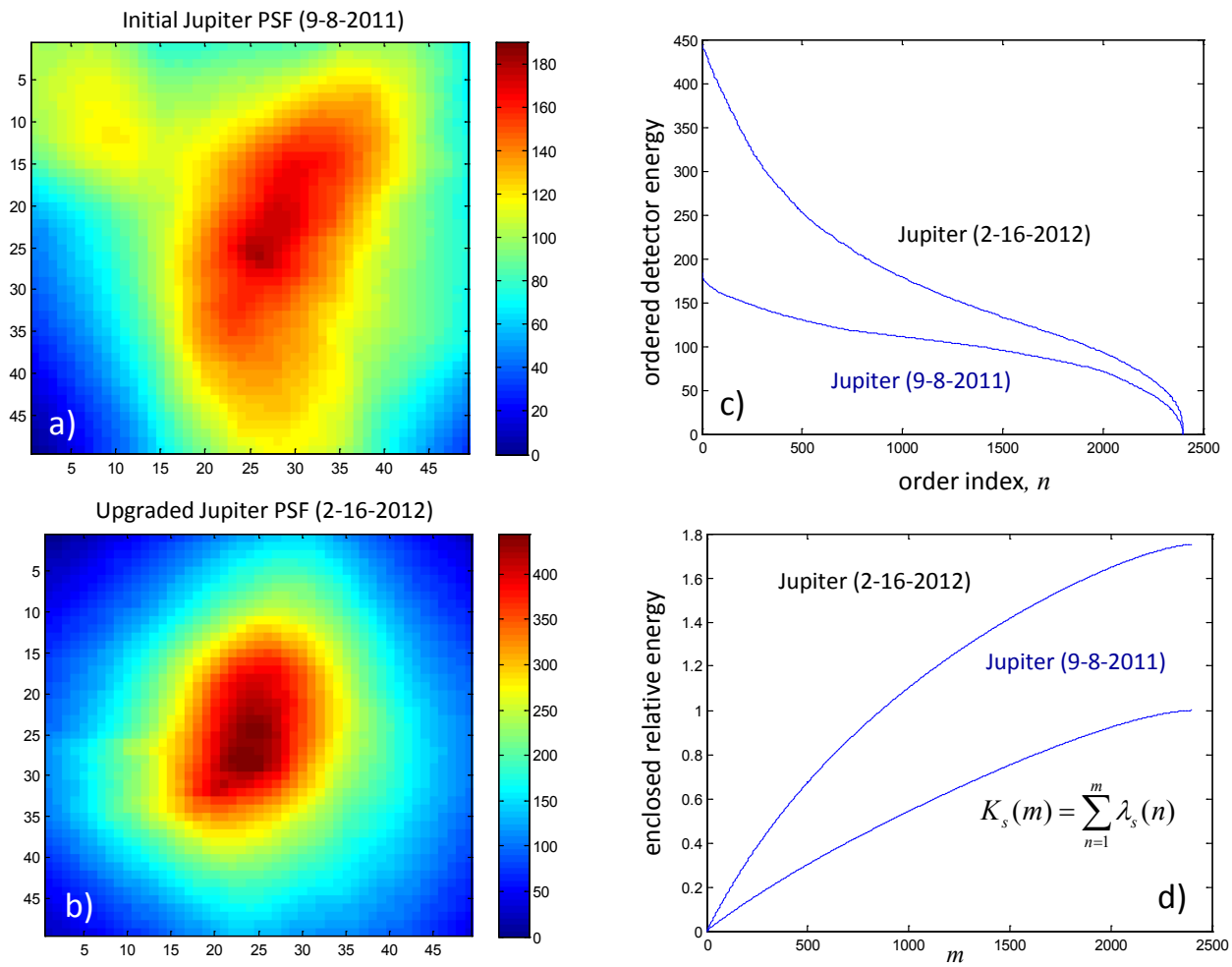

Figure 6. Comparison of point spread functions generated by the initial and upgraded panel mounting structures: a) Jupiter PSF obtained initially on 9/8/2011; b) improved Jupiter PSF after implementing upgrades to the panel mounting structure (2/16/2012); c) performance improvement quantified in terms of ordered detector energies; d) increased signal energy as a function of m due to better light concentration by the upgraded panel mounting structure.

The true PSF generated by Jupiter on February 16th was actually somewhat better than that shown in Fig. 6a, because light seeping through gaps in the main reflector from the control room (which was directly behind Jupiter and about 250 yards distant during this track) caused some horizontal intensity streaks on the left side, which was a peculiarity of this particular Jupiter track and is not expected to impact future tracks.

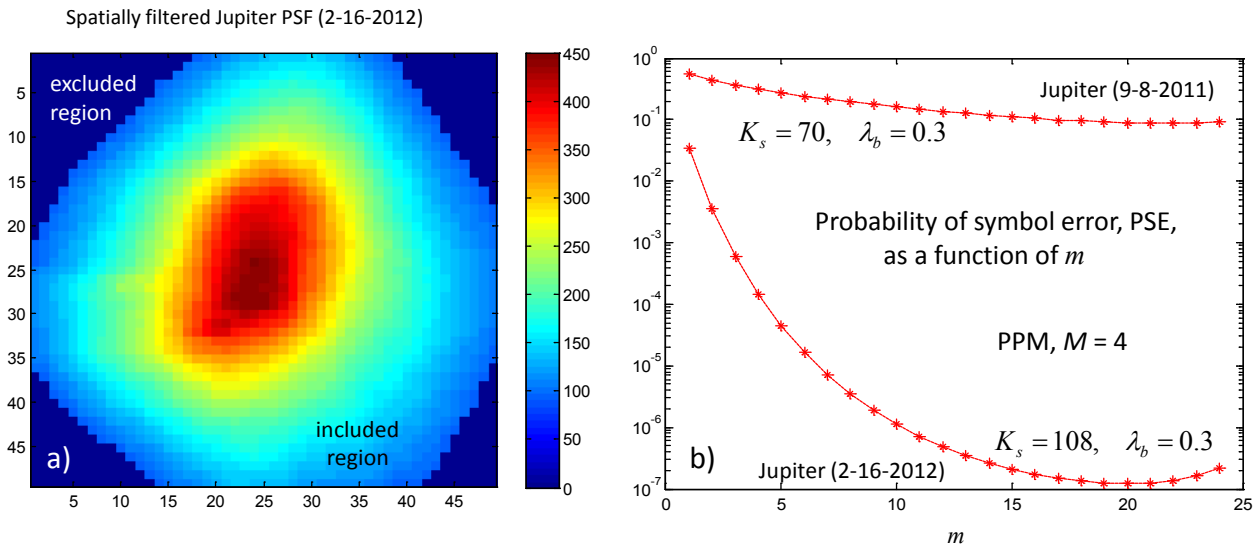

Figure 7. Comparison of Vertex polished panel communications performance, before and after the mounting structure was improved: a) spatially filtered PSF showing the excluded regions at the four corners of the sensor; b) illustrating the dramatic decrease in symbol error probability after the mounting structure upgrades have been implemented.

The polished panel's symbol error probability performance is compared in Fig. 7, which clearly shows the dramatic decrease in the symbol error probability following the successful upgrades, due to substantially greater collected signal energy and better concentration, resulting in more effective rejection of background interference. The action of the optimal (1, 0) spatial filter designed to limit background energy is evident in Fig. 7a, effectively eliminating background energy from the four corners of the detector array where signal energy is at a minimum. The average collected signal energy has been increased from 70 photons per PPM symbol to 108 photons due to better signal concentration, and at the same time the total background interference has been reduced, yielding symbol error probability of $PSF = 1.1 \times 10^{-7}$ for the case of the improved PSF, instead of $PSF = 8 \times 10^{-2}$ as obtained with the original configuration. This example clearly illustrates the dramatic improvements enabled by the recently concluded upgrades in the Vertex polished panel mounting structure.

V. SUMMARY AND CONCLUSIONS

Installation, upgrades and initial evaluation of a custom built polished aluminum panel intended for optical communications via hybrid 34-meter DSN antennas has been described in this paper. It was shown that high-quality aluminum panels can be manufactured with surface accuracies sufficient to concentrate light into a small spot, that could be detected with large area photon-counting arrays in the future. As part of this demonstration effort, an aluminum panel manufactured by Vertex Antennentechnic GmbH. was installed on the main reflector of the 34-meter antenna at DSS-13, and a large-sensor camera manufactured by Finger Lakes Instruments was installed into a weather-proof enclosure and mounted next to the subreflector, to record the point-spread function (PSF) generated by

the polished panel. Data was collected while tracking the planet Jupiter at night, which provided sufficient illumination to produce detailed images of the PSF with various antenna pointing offsets [2], facilitating the evaluation of future optical communications performance. A mathematical model of the focal-plane energy distribution was developed and applied to the experimentally measured PSF in order to predict optical communications performance. It was noted that significant distortions were present in the PSF when it was first centered over the sensor, the result of mechanical stress on the polished panel introduced by the mounting structure. The panel mounting structure was therefore upgraded following initial installation to minimize mechanical distortions, leading to dramatic improvements in the PSF, which were evaluated and quantified in terms of the communications performance that a future polished panel optical receiver could achieve.

VI. REFERENCES

[1] V. Vilnrotter, D. Hoppe, B. Moision, J. Charles, "Optical Communications Performance of Hybrid 34-meter Microwave Antennas," IEEE Aerospace Conference, Big Sky, MT, March 2010.

[2] V. Vilnrotter, "Experimental Evaluation of Optically Polished Panels on the Deep Space Network's 34 Meter Antenna," IEEE Aerospace Conference, Big Sky, MT, March 2012.

[3] V. Vilnrotter, M. Srinivasan, "Adaptive Detector Arrays for Optical Communications Receivers," IEEE Transactions on Communications, Vol. 50, Issue 7, 2002, pp. 1091-1097.

Acknowledgments: The author would like to acknowledge the contributions of team members Daniel Hoppe, Theodore Hanson, Asim Sehic, and Philip Tsao for fabricating and installing the polished panels, camera enclosure and computer interface on the DSS-13 antenna.

The research described in this paper was carried out at the Jet Propulsion Laboratory, California Institute of Technology, under a contract with the National Aeronautics and Space Administration.